Abrupt transition from slow to fast melting of ice

Rui Yang [1], Kai Leong Chong [2,1,*] Hao-Ran Liu [1], Roberto Verzicco [1,3,4]
and Detlef Lohse [1,5,†]

[1]*Physics of Fluids Group and Max Planck Center for Complex Fluid Dynamics,*
and J. M. Burgers Centre for Fluid Dynamics, University of Twente,
P.O. Box 217, 7500AE Enschede, The Netherlands
[2]*Shanghai Key Laboratory of Mechanics in Energy Engineering,*
Shanghai Institute of Applied Mathematics and Mechanics,
School of Mechanics and Engineering Science, Shanghai University, Shanghai,
200072, People's Republic of China
[3]*Dipartimento di Ingegneria Industriale, University of Rome "Tor Vergata," Rome 00133, Italy*
[4]*Gran Sasso Science Institute, Viale F. Crispi, 7 67100 L'Aquila, Italy*
[5]*Max Planck Institute for Dynamics and Self-Organization, 37077 Göttingen, Germany*

How fast ice melts in turbulent flows is key to many natural and industrial processes, most notably the melting of ice in the polar regions. To get a better quantitative understanding of the physical mechanics at play, as a model system we pick vertical convection, consisting of ice and fresh water, and examine the lateral melting behavior through numerical simulations and theory. We find that the melting rate of ice as a function of an increasing heating temperature undergoes an abrupt transition from a slow- to a fast-melting state, contrary to the intuition of a gradual transition. The abrupt transition of the ice melting rate is due to the emergence of a reversed buoyant flow, due to the density anomaly of water near the melting point. A theoretical model based on energy conservation gives rise to a universal expression to relate the global heat fluxes and the ice melting rate which is consistent with our data. Besides their fundamental significance, our findings improve our understanding of how phase transitions couple to adjacent turbulent flow.

I. INTRODUCTION

Ice melting has great relevance in oceanography [1,2], meteorology [3,4], and geophysics [5,6]. The most relevant example may be the melting of ice in rivers and lakes and polar regions, e.g., subglacial lakes [2,7], ice floes [8], and melt ponds [9]. Melt ponds absorb significantly more solar energy than the surrounding ice leading to accelerated melting. This process is known as positive feedback of albedo [10]. It is presently ignored in the global climate models, which could be a reason why the present models underestimate the sea ice's rapid decline [11,12]. The melting process, which involves a phase transition, also applies to various industrial applications, such as freezing of a liquid in pipe flows [13] and heat storage of phase-change materials [14,15]. The interaction between phase transition processes and turbulent flows is thus an interesting and complicated problem with wide applications [16–19]. Such dynamics for a liquid out of equilibrium often leads to fascinating phenomena [20], with very different melting behavior as compared to that in quiescent fluids.

*klchong@shu.edu.cn
†d.lohse@utwente.nl

Previous work has thoroughly investigated the melting in convective flows with density linearly depending on temperature [21–23]. However, in reality, the density of fresh water exhibits anomalous thermodynamic behavior when its temperature is near the melting point. Specifically, freshwater is the densest at about $4\,°C$, which is the case for ice melting in rivers and lakes [24] and many industrial applications, e.g., pipe flow [13]. On the one hand, for melting processes in Rayleigh-Bénard (RB) convection [25–28], which is a fluid layer confined between a cold top plate and a hot bottom plate, some of the early systematic studies focus on fluid motions and different regimes of pattern formation [29,30]. The pioneering work of Wang *et al.* [31] identified distinct regimes of the flow pattern and ice morphology, and investigated the stable ice front thickness after reaching the statistical equilibrium state. On the other hand, in the case of melting with a stable ice surface in vertical convection [32,33], which is a fluid layer with one side cooled and the other heated, experimental studies [34–36] have found a significant suppression of the heat transfer due to the density anomaly. Recent experimental and numerical studies also focus on the equilibrium state of the ice front in vertical convection [24,37]. However, the *time-dependent* dynamics of ice melting in convective flows with a density anomaly has not yet been understood, especially not when the melting is coupled to turbulent flow.

In this paper, we conduct numerical simulations of the melting process in an ice-water system in the geometry of vertical convection (one side cooled, the other heated) in order to reveal and highlight the nontrivial effect of the density anomaly on the transient ice melting process. On increasing the heating temperature, an abrupt transition from a slow- to a fast-melting state is observed when the anomalous property of water density is considered. In contrast, this striking and abrupt transition does not exist when the density anomaly is absent. Despite the complexity in the phase transition and its interaction with the turbulent convective flow, we found that a parameter-free theoretical model based on energy conservation correctly and quantitatively predicts the melting rate and its abrupt transition.

II. SIMULATION DETAILS

In the simulations, we consider the real water density property near $4\,°C$ given as $\rho = \rho_0(1 - \beta^*|T - T_{\max}|^q)$, where β^* is the generalized thermal expansion coefficient, with the exponent $q = 1.895$ and $T_{\max} = 4\,°C$ [31,38–40]. For comparison, simulations without the density anomaly are carried out with the Boussinesq approximation as $\rho = \rho_0[1 - \beta(T - T_0)]$, where β is the standard thermal expansion coefficient, and ρ_0 and T_0 are the reference density and temperature, respectively.

The simulations are carried out using the phase-field approach, commonly used to study melting and solidification processes [41], which we dynamically couple to the Navier-Stokes equations [23,42]. Comparisons to the results from other experiments and simulations act as validation for our results. The phase field method is implemented in a direct numerical simulation solver for the Navier-Stokes equations, namely, AFiD, which is a second-order finite-difference solver, open sourced by our research group, to simulate melting of solids immersed in a fluid flow. This method includes a phase function ϕ with the value 0 in solid and 1 in liquid. The governing equations include the momentum equation, the heat equation, and the phase-field equation:

$$\frac{\partial u_i}{\partial t} + u_j\frac{\partial u_i}{\partial x_j} = -\frac{\partial p}{\partial x_i} + |\theta - \theta_{\max}|^q \delta_{iz} + \sqrt{\frac{\mathrm{Pr}}{\mathrm{Ra}}}\frac{\partial^2 u_i}{\partial x_j^2} - \frac{(1-\phi)^2 u_i}{\eta}, \tag{1}$$

$$\frac{\partial \theta}{\partial t} = -u_i\frac{\partial \theta}{\partial x_i} + [1 + (\lambda - 1)(1 - \phi)]\sqrt{\frac{1}{\mathrm{RaPr}}}\frac{\partial^2 \theta}{\partial x_j^2} - \frac{1}{\mathrm{St}}\frac{dQ(\phi)}{d\phi}\frac{d\phi}{dt}, \tag{2}$$

$$\frac{\partial \phi}{\partial t} = M\nabla^2\phi + \mathrm{St}\frac{\alpha M}{\epsilon}(\theta - \theta_m)\frac{dp}{d\phi} - \frac{M}{4\epsilon^2}\frac{dG(\phi)}{d\phi}. \tag{3}$$

The main dimensionless control parameter is the Rayleigh number Ra^* (with the density anomaly effect) or Ra (without the density anomaly effect), and the density inversion parameter $\theta_{\max}$, defined

as

$$\text{Ra}^* = \frac{\beta^* g H^3 (T_h - T_c)^q}{\nu \kappa}, \quad \text{Ra} = \frac{\beta g H^3 (T_h - T_c)}{\nu \kappa}, \quad \theta_{\max} = \frac{T_{\max} - T_c}{T_h - T_c}, \tag{4}$$

where T_h, T_c are the dimensional temperatures of the heated wall and the cooled wall, respectively, which are a distance H apart. ν and κ are the kinematic viscosity and thermal diffusivity of the liquid, respectively, and g the gravitational acceleration.

Next to the Rayleigh number, the other most relevant dimensionless number of this process is the Stefan number $\text{St} = C_p (T_h - T_c)/\mathcal{L}$, which measures the ratio of sensible to latent heat, where C_p is the isobaric heat capacity of water and $\mathcal{L}$ is the latent heat of melting. Here we fix $T_c = 0\,^\circ\text{C}$, the same as the melting point, and the domain width $H = 0.2$ m is a common length scale of melt ponds [43,44] and in experiments [31,45]. In the simulations we vary the dimensional control parameter T_h from $4\,^\circ\text{C}$ to $20\,^\circ\text{C}$ (correspondingly the dimensionless control parameters $4.8 \times 10^7 < \text{Ra}^* < 1 \times 10^9$, $1.4 \times 10^7 < \text{Ra} < 6.9 \times 10^7$, and $0.05 < \text{St} < 0.25$). We express the result in terms of the dimensionless temperature θ, defined as $\theta = (T - T_c)/(T_h - T_c)$. We emphasize that varying Ra and St can independently affect the results: Increasing Ra (with fixed St) will increase the level of turbulence and more interactions between the small-scale flow structures and the ice interface will occur, while changing St (with fixed Ra or Ra*) will change the timescale ratio between the turnover time of the convective flow (sensible heat) and the timescale of evolution (latent heat). The further dimensionless control parameters are the Prandtl number Pr (water property), the conductivity ratio $\lambda = \kappa_{\text{ice}}/\kappa$, and the aspect ratio Γ, which are fixed as $\text{Pr} = 10$ (cold water), $\lambda = 7$, and $\Gamma = 1$.

The applied phase-field model was initially derived based on entropy conservation, which guarantees the thermodynamic consistency and also satisfies the Gibbs-Thompson relation [42]. Different choices of the parameters are tested to ensure the convergence. We refer to the choice of parameters as in [23], which we also use in our work, including the mobility $M = 1/\sqrt{\text{Ra}\text{Pr}}$ and coupling parameter $\alpha = \text{St}/\epsilon$, to minimize the error for a given spatial resolution, the function $G(\phi) = \phi^2 (1 - \phi)^2$ is a double-well potential function, and $Q(\phi) = \phi^3 (10 - 15\phi + 6\phi^2)$ is a smoothing function to ensure a smooth transition between the solid and liquid phase. See more details in [23]. ϵ is proportional to the numerical grid size, and $\eta = 0.001$ is a small enough to ensure that the velocity in the solid phase quickly decays to zero.

III. VALIDATIONS

A. Comparison to experiments and numerical simulations in Ref. [31]

We compared the result of our DNS code to the experiments and numerical simulations from Wang *et al.* [31], where the ice freezes in fresh water from the top with fixed temperature below the freezing point. The bottom plate is heated, so that finally an equilibrium state is reached with a certain ice layer height. For the validation, we run 2D simulations with the same control parameters as in [31], namely, $\text{Pr} = 1$, $9.5 \times 10^8 < \text{Ra}^* < 5.4 \times 10^9$, with a grid number of 576×576. The Stefan number is fixed to $\text{St} = 1$ since St has hardly any effect on the equilibrium state, but this value allows for faster convergence, because smaller St means smaller timescale separation between the flow and the interface dynamics. The results for the equilibrium ice layer height are shown in Fig. 1. They are in good agreement with both the experiments and the numerical simulations of Wang *et al.* [31].

B. Comparison to other numerical simulations

Next, we compared the result of our DNS code with the results of Ulvrová *et al.* [6] in a square geometry with the melting of a solid block at the upper cold plate in a Rayleigh-Bénard setup; see Fig. 2(a). The temperatures of the bottom boundary and top boundary are fixed as $T_b = 1$ and $T_t = 0$. The melting temperature is maintained as $T_m = 0.5$. Vertical walls are insulating, and no-slip boundary conditions are applied on all boundaries. Our simulation was performed in the same
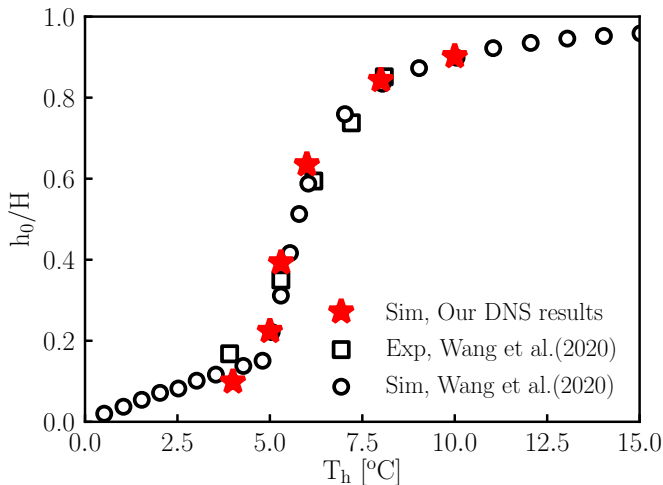
FIG. 1. The normalized equilibrium ice-water interface height as a function of the heating temperature T_h: comparison of our numerical results with the prior experiments and numerical simulations by Wang *et al.* [31].

geometry as in Ref. [6] and with the same parameters, namely, St = 0.1, Ra = 10^5, and Pr = 1000, with a grid with 128×128 grid points. The comparison of the time evolution of the mean Nusselt number over the bottom boundary is shown in Fig. 2(b). The comparisons of the vertical temperature profiles at $x = 0.25$ in the horizontal direction for four different times between the reference and our result are shown in Fig. 3. All these comparisons between our calculations and those of Ref. [6] show good agreement, further validating our code.

We also compared the result of our DNS code with the results of Ref. [6] in a square enclosure heated from the left vertical wall with fixed temperature $T_h = 1$, and cooled from the right vertical wall with fixed temperature $T_c = 0$, and the horizontal walls are kept insulated; see Fig. 4(a). The melting temperature is $T_m = 0$. After an initial state of pure conduction, natural convection starts in the liquid phase and results in faster melting in the upper part of the cavity.
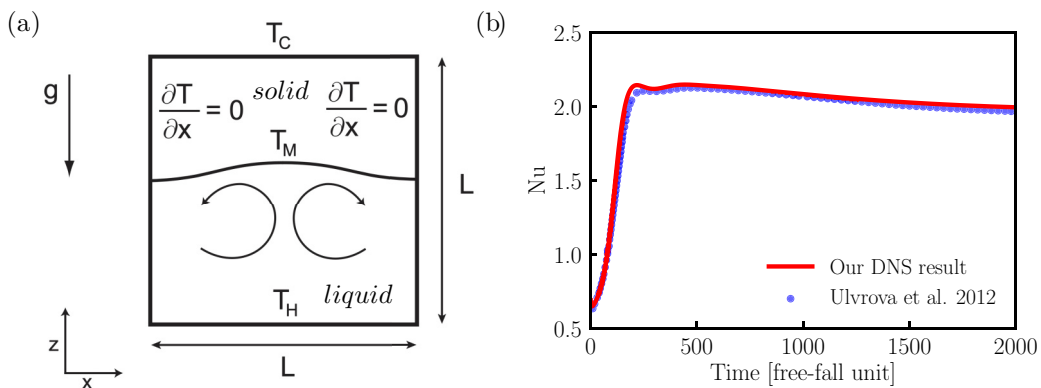

FIG. 2. (a) The schematic sketch of the setup of melting in Rayleigh-Bénard convection from Ulvrova *et al.* [6]. (b) Comparison of the time evolution of the mean Nusselt number over the hot bottom boundary between the results of Ulvrova *et al.* [6] and our results.
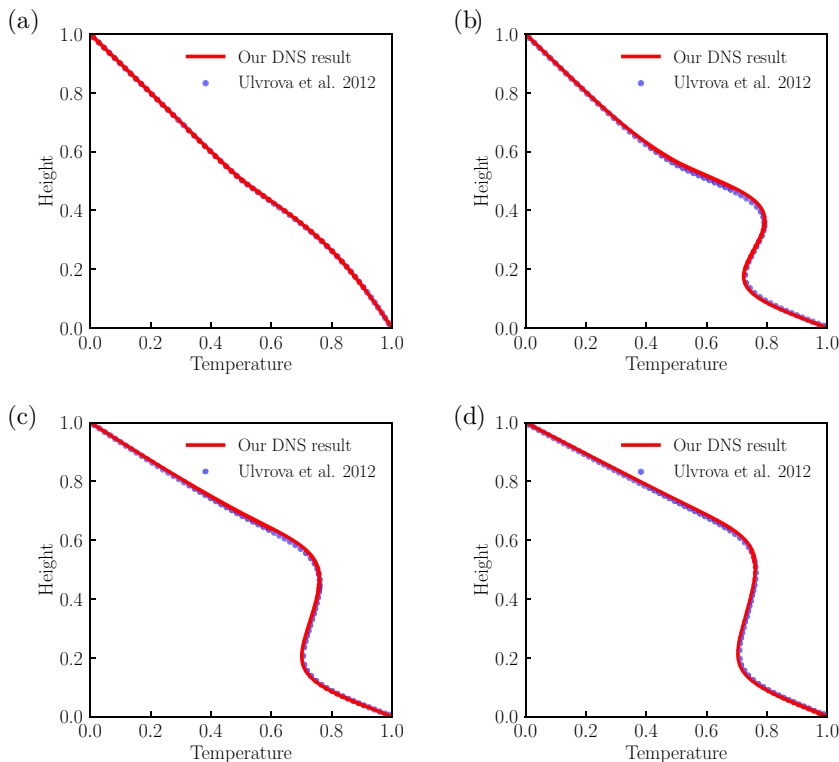
FIG. 3. Vertical profiles of the temperature at $x = 0.25$ (in the horizontal direction) for four different times (a) $t = 200$, (b) $t = 2000$, (c) $t = 10\,000$, and (d) $t = 20\,000$ in free-fall time units. Solid red lines represent our simulation results. Blue points represent the results from Ulvrova et al. [6].

IV. FLOW STRUCTURES

Two- and three-dimensional simulations are conducted in a square or box domain [see Fig. 5(a)]. The temperature at the left and right plate is fixed as T_h and T_c, while the other plates are adiabatic and all boundaries are no-slip and impermeable. Initially, the domain is entirely filled with ice at the
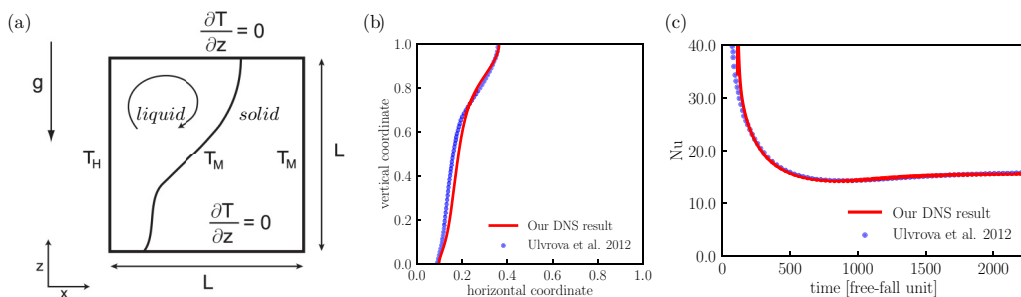

FIG. 4. (a) Schematic sketch of the setup of melting in vertical convection from Ulvrova et al. [6]. (b) The comparison of the interface position at time $t = 2236$ free-fall time units ($t = 0.1$ diffusive time unit). (c) Comparison of the time evolution of the mean Nusselt number over the hot bottom boundary between the results of Ulvrova et al. [6] and our results.
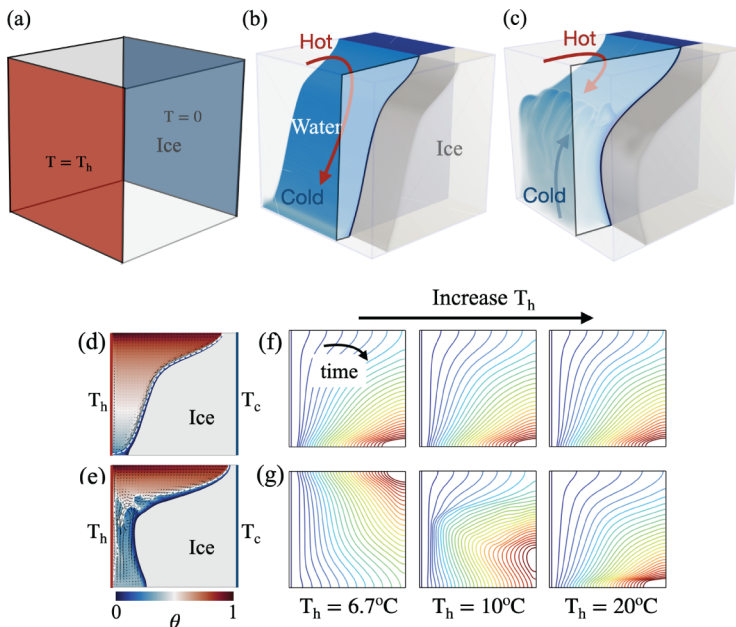
FIG. 5. 3D visualization of (a) the simulation setup and the instantaneous temperature field at $T_h = 10\,°\text{C}$ (b) without and (c) with density anomaly. The 2D instantaneous temperature field at $T_h = 10\,°\text{C}$ (d) without and (e) with a density anomaly, where the white dashed line shows the contour of $T_x = 4\,°\text{C}$. The solid-liquid interface evolution (f) without and (g) with density anomaly at $T_h = 6.7,\ 10,\ 20\,°\text{C}$, correspondingly to $\text{Ra}^* = 1.25 \times 10^8,\ 2.7 \times 10^8,\ 1 \times 10^9$.

melting point $T = 0$. As time evolves, the melting starts from the left, heated wall. The initial stage of melting is dominated by pure conduction, and then convection sets in.

The resultant convective flow structures are quite different, depending on whether or not the density anomaly is considered. The differences in ice morphology and flow structures are shown in Figs. 5(b) and 5(c) for three dimensions and Figs. 5(d) and 5(e) for two dimensions (see the Supplemental Material [46] for movies of ice morphology and flow structure evolution). In a nutshell, the density anomaly can lead to rising cold thermal plumes and to a different ice morphology with a thicker ice layer at midheight instead of at top and bottom, as seen from both the 3D and 2D simulations. We further display how the shape of the ice-water interface evolves with time in Figs. 5(f) and 5(g). Without the density anomaly, the ice shape evolves similarly for various heating temperatures T_h. In contrast, with the density anomaly, the morphological change of the interface can enter different scenarios depending on T_h. One can basically identify three main types:

(1) At high enough temperatures of the heated plate, e.g., $T_h = 20\,°\text{C}$, the ice melts faster from the top, similarly to the case without density anomaly. Adjacent to the ice block, the large-scale circulation brings the relatively warm fluid downwards, resulting in a faster melting rate near the top.

(2) In the other extreme when the temperature at the heated plate is relatively close to $4\,°\text{C}$ (temperature with maximum density), e.g., $T_h = 6.7\,°\text{C}$, the ice melts faster near the bottom. In this case, the circulation direction is reversed, because of less dense fluid in the proximity of the ice.

(3) At intermediate temperatures, however, e.g., for $T_h \approx 10\,°\text{C}$, a transitional ice morphology exists [see middle figure in Fig. 5(g)]. In this case, competing local circulations occur instead of a prevailing large-scale circulation, giving rise to a fairly convex ice morphology, which evolves with time.
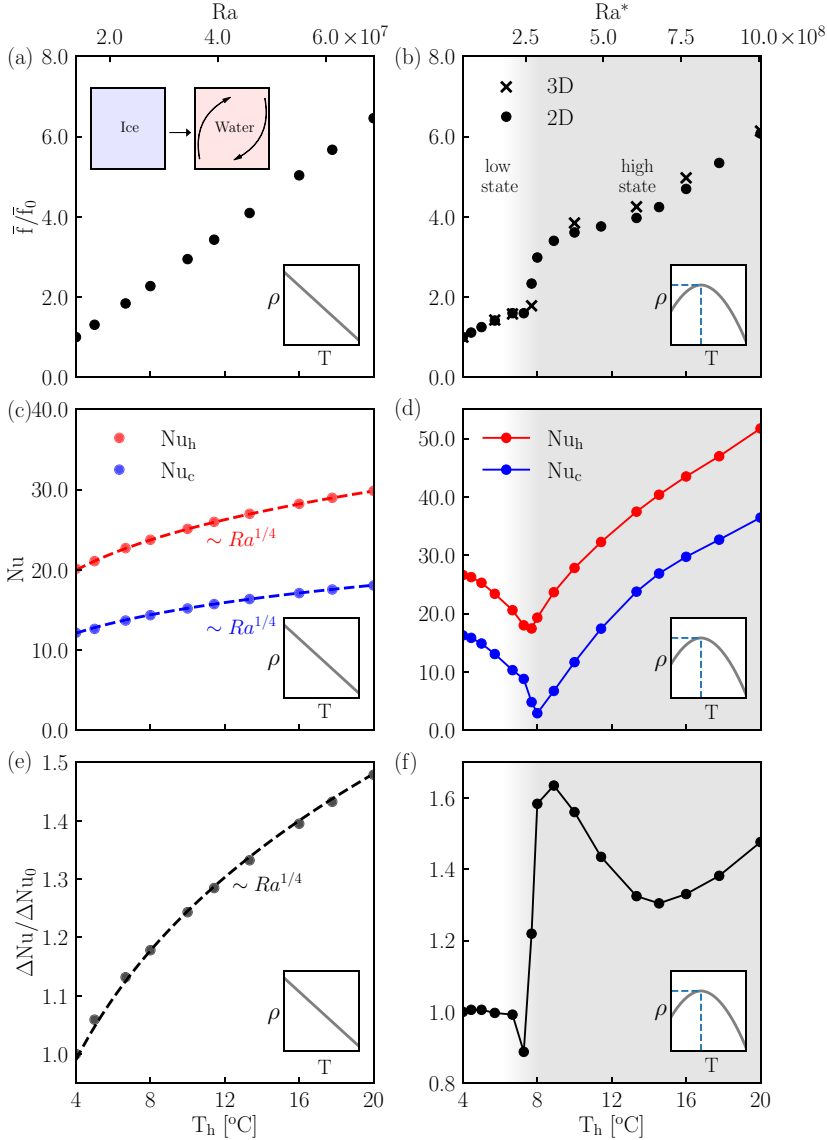
FIG. 6. The overall melting rate $\overline{f}$ (calculated from the characteristic length scale and time from completely ice to completely water), normalized by the overall melting rate at $4\,^\circ\mathrm{C}$, as a function of T_h (a) without density anomaly and (b) with density anomaly. (c), (d) Overall averaged Nu_h and Nu_c, as a function of T_h (c) without and (d) with density anomaly. (e), (f) Net heat flux $\Delta\mathrm{Nu}$, normalized by the net heat flux at $4\,^\circ\mathrm{C}$, as a function of T_h (e) without and (f) with density anomaly. The darker shaded part shows the region of high-melting state.

V. MELTING RATE

Given the intriguing morphological change, one wonders about its effect on the melting rate. When the density anomaly is neglected as depicted in Fig. 6(a), the melting rate is linear with T_h as one may have intuitively expected. However, with the density anomaly, the melting rate undergoes a sharp increase by 100% at $T_h \approx 8\,^\circ\mathrm{C}$, with a low melting state below $T_h \approx 8\,^\circ\mathrm{C}$, and a high one above [see Fig. 6(b)]. This finding is highly nontrivial as one clearly would expect a gradual increase in melting rate with increasing heating temperature.
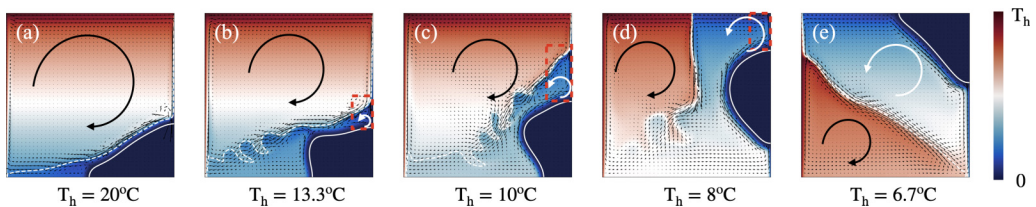
FIG. 7. The flow and temperature field for $T_h = 20$, 13.3, 10, 8, and 6.7 °C for water with the density anomaly, where the white dashed line shows the contour line of $T = 4$ °C and the solid white line the solid-liquid interface. The black and white curved arrows indicate the clockwise large-scale circulation and the reversed buoyant flow. The red dashed boxes shown in (b) and (c) capture the region near the cooled plate where the shielding of buoyant reversal flow takes effect, which clearly explains the ΔNu change and the melting rate.

To find the origin of this transitional behavior of ice melting, we further measure the Nusselt numbers (dimensionless heat transfer) at both the heated and the cooled plate, Nu_h and Nu_c. As key quantities of melting, Nu_h and Nu_c represent the heat fluxes in and out of the domain, which directly relate to the melting rate. For cases without the density anomaly shown in Fig. 6(c), both Nu_h and Nu_c follow the well-known 1/4 scaling with Ra [32]. However, a nonmonotonic trend is observed for cases with the density anomaly [see Fig. 6(d)], where Nu first decreases to a minimum, followed by an increasing trend. Previous studies [35] had also empirically observed this nonmonotonic trend caused by the density anomaly; however, its effect on the melting rate was not yet understood. Here, by closely inspecting Nu_h and Nu_c, we actually see that Nu_c can reach much lower values than Nu_h, leading to a net heat flux $\Delta Nu = Nu_h - Nu_c$ to enhance the melting. This net heat flux dramatically increases at $T_h \approx 8$ °C [Fig. 6(f)] compared to the ΔNu without the density anomaly [Fig. 6(e)].

Why is the heat flux Nu_c into the cooled wall largely suppressed in the case with the density anomaly? We answer this question by looking into the local flow structure (Fig. 7). As the heating temperature T_h progressively decreases, a reversed buoyant flow emerges due to the density anomaly, since the warmer fluid is heavier and descends, while the cooler fluid near the melting front is lighter and rises. The reversed buoyant flow counteracts the pre-existing large-scale circulation driven by vertical convection [Figs. 7(a)–7(d)]. For relatively large T_h ($T_h \geqslant 8$ °C), the reversed buoyancy drives cold melt fluid upward from the ice block. In this case, cooler water adjacent to the ice block has been carried by the reversed flow to the cooled plate, which shields the cooler plate from the large temperature contrast and thus suppresses the heat flux, similarly as in low aspect ratio $\Gamma \ll 1$ RB flow, where staggered convection rolls can also provide only small heat flux [47]. This shielding effect eventually vanishes when the ice block locates at the top when T_h gets closer to 4 °C [Fig. 7(e)].

VI. RELATION BETWEEN HEAT FLUX AND MELTING RATE

Since we have observed enhancement both of the heat flux difference ΔNu and of the melting rate $\bar{f}$, we are wondering whether one can quantify a relation between these two response quantities of the system. To do so, we employ a theoretical model based on energy conservation. Following the derivation from Favier *et al.* [23], by integrating the energy equation over the whole volume V, we find the following relation:

$$\sqrt{\frac{1}{RaPr}}\left(\int_{\text{heated}} \theta_z \, dA - \int_{\text{cooled}} \theta_z \, dA\right) = \frac{d}{dt}\int_V \theta \, dV + \frac{d}{dt}\int_V [St^{-1}Q(\phi)] \, dV, \qquad (5)$$

where $Q(\phi)$ represents the interpolation function for energy. The left-hand-side terms correspond to the surface integral of the heat fluxes entering and leaving the domain, and the right-hand-side terms
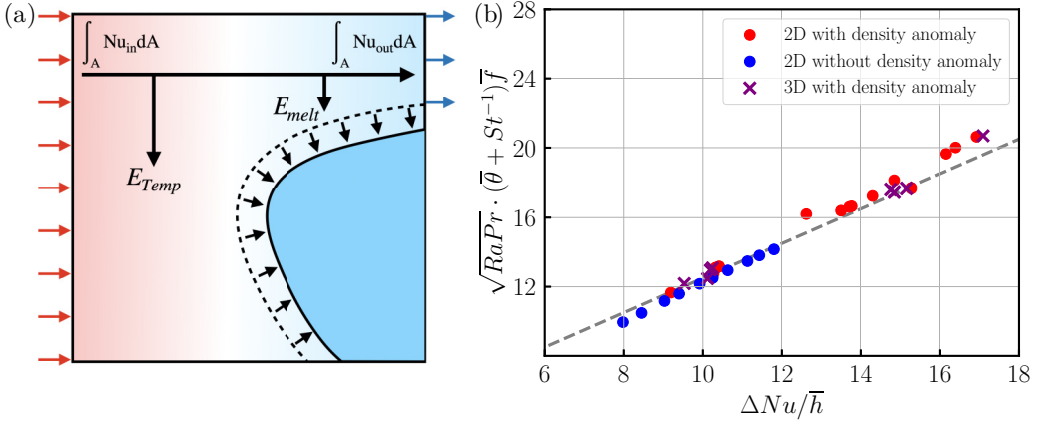
FIG. 8. (a) Illustration of the heat flux into and out of the domain during the melting process. (b) Plot of the relation between the effective net heat flux $\Delta Nu/\overline{h}$ and the renormalized melting rate $\sqrt{RaPr}(\overline{\theta} + St^{-1})\overline{f}$. The dashed line represents the linear fitting curve according to Eq. (6) with slope 1 and intercept 3.0.

correspond to the total rate of change of the enthalpy in the system, which is constituted by changing the bulk fluid temperature and the latent heat due to melting; see the illustration in Fig. 8(a).

Equation (5) can be further simplified as

$$\sqrt{\frac{1}{RaPr}}\frac{\Delta Nu}{\overline{h}} \approx (\overline{\theta} + St^{-1})\overline{f}, \tag{6}$$

where $\Delta Nu/\overline{h} = (Nu_h - Nu_c)/\overline{h}$ is the effective net heat flux, $\overline{h}$ is the mean distance from the ice interface to the heated plate, $\overline{f} = 1/\overline{\tau}$ is the overall melt rate, and $\overline{\tau}$ is the time for complete ice melting. The volume integral of the temperature is replaced by the mean temperature $\overline{\theta}$, assuming that the change of $\overline{\theta}$ over time is negligible.

The obtained expression (6) for the melting rate and how it depends on ΔNu, St, and $\overline{\theta}$ is the main quantitative result of this paper. We plot $\sqrt{RaPr}(\overline{\theta} + St^{-1})\overline{f}$ vs $\Delta Nu/\overline{h}$ using all simulation data (with and without density anomaly, 2D and 3D) [see Fig. 8(b)]. Despite the complicated flow structures and nontrivial trend for the melting speed and the heat flux, the data nicely follow Eq. (6) apart from small deviations caused by approximating the temporal change of the global temperature. Therefore, in spite of the density anomaly, a simple relation can link the key quantities (ΔNu and $\overline{f}$) of melting, based on energy conservation.

VII. CONCLUSIONS

In conclusion, we have shown that the melting rate of ice adjacent to turbulent convection exhibits an abrupt transition upon increasing the heating temperature because of the density anomaly of water. The physical origin of this abrupt transition is the emergence of reversed buoyant flow, causing a shielding effect to the cooled plate. We have also checked the effect of the aspect ratio on the overall flow pattern by performing simulations for a larger aspect ratio ($\Gamma = 2$) cell, qualitatively finding the same effects and in particular reversed buoyant flow. It is noted that, although density anomaly effects on turbulent convection have been studied as early as Veronis [48], the strong nonlinear enhancement of the melt rate and the sharp transition in the flow pattern are remarkable. They originate from the complicated interaction between the melting process and the turbulent flow. Finally, we have shown the robustness of the derived balance equation. It enables the estimation of the melting rate from the global heat flux, without considering the complicated turbulent flow inside. Our findings of the effect of the density anomaly of water on the ice morphology and the

melt rate can be directly applied to freshwater systems, e.g., melt ponds, lake ice, and subglacial lakes. Note, however, that the Ra numbers for whole glacier shelves will be much higher and not achievable in our DNS. In addition, for glacier shelve melting also the salt dissolved in the ocean plays an important role.

Looking beyond fresh water, in industrial applications, there are far more examples of liquids with a density anomaly, such as silicon, phosphorus, CO_2 [49], etc. The unveiled flow physics enables the generalization of our findings to these fluids, and an extension of the study to a larger parameter range in the four-dimensional parameter space (Ra, St, Pr, Γ) is clearly desirable. Beyond that, future studies on multicomponent liquid should be extended to seawater, as for glacier melting in seawater, the temperature corresponding to the density maximum is altered by the salt concentration, which in turn influences the likelihood of buoyant flow reversal. In fact, in that case both temperature and concentration effects on the density must be considered. Here abrupt transitions may act as tipping points with potentially huge consequences for the climate [50,51].

[1] L. Ristroph, Sculpting with flow, J. Fluid Mech. **838**, 1 (2018).

[2] L.-A. Couston and M. Siegert, Dynamic flows create potentially habitable conditions in Antarctic subglacial lakes, Sci. Adv. **7**, eabc3972 (2021).

[3] T. Alboussiere, R. Deguen, and M. Melzani, Melting-induced stratification above the Earth's inner core due to convective translation, Nature (London) **466**, 744 (2010).

[4] F. E. Butcher, M. R. Balme, C. Gallagher, N. S. Arnold, S. J. Conway, A. Hagermann, and S. R. Lewis, Recent basal melting of a mid-latitude glacier on Mars, J. Geophys. Res. Planets **122**, 2445 (2017).

[5] R. I. Woolway, B. M. Kraemer, J. D. Lenters, C. J. Merchant, C. M. O'Reilly, and S. Sharma, Global lake responses to climate change, Nat. Rev. Earth Environ. **1**, 388 (2020).

[6] M. Ulvrová, S. Labrosse, N. Coltice, P. Raback, and P. Tackley, Numerical modelling of convection interacting with a melting and solidification front: Application to the thermal evolution of the basal magma ocean, Phys. Earth Planet. Inter. **206–207**, 51 (2012).

[7] L.-A. Couston, Turbulent convection in subglacial lakes, J. Fluid Mech. **915**, A31 (2021).

[8] E. W. Hester, C. D. McConnochie, C. Cenedese, L.-A. Couston, and G. Vasil, Aspect ratio affects iceberg melting, Phys. Rev. Fluids **6**, 023802 (2021).

[9] P. Popović, B. Cael, M. Silber, and D. S. Abbot, Simple Rules Govern the Patterns of Arctic Sea Ice Melt Ponds, Phys. Rev. Lett. **120**, 148701 (2018).

[10] M. M. Holland, C. M. Bitz, and B. Tremblay, Future abrupt reductions in the summer Arctic sea ice, Geophys. Res. Lett. **33**, L23503 (2006).

[11] M. M. Holland and J. A. Curry, The role of physical processes in determining the interdecadal variability of central Arctic sea ice, J. Clim. **12**, 3319 (1999).

[12] J. Stroeve, M. M. Holland, W. Meier, T. Scambos, and M. Serreze, Arctic sea ice decline: Faster than forecast, Geophys. Res. Lett. **34**, L09501 (2007).

[13] M. Epstein and F. Cheung, Complex freezing-melting interfaces in fluid flow, Annu. Rev. Fluid Mech. **15**, 293 (1983).

[14] M. M. Farid, A. M. Khudhair, S. A. K. Razack, and S. Al-Hallaj, A review on phase change energy storage: Materials and applications, Energy Convers. Manage. **45**, 1597 (2004).

[15] A. Sharma, V. V. Tyagi, C. Chen, and D. Buddhi, Review on thermal energy storage with phase change materials and applications, Renewable Sustainable Energy Rev. **13**, 318 (2009).

[16] L. Ristroph, M. N. Moore, S. Childress, M. J. Shelley, and J. Zhang, Sculpting of an erodible body by flowing water, Proc. Natl. Acad. Sci. USA **109**, 19606 (2012).

[17] J. M. Huang, M. N. J. Moore, and L. Ristroph, Shape dynamics and scaling laws for a body dissolving in fluid flow, J. Fluid Mech. **765**, R3 (2015).

[18] M. S. Davies Wykes, J. M. Huang, G. A. Hajjar, and L. Ristroph, Self-sculpting of a dissolvable body due to gravitational convection, Phys. Rev. Fluids **3**, 043801 (2018).

[19] J. M. Huang, J. Tong, M. Shelley, and L. Ristroph, Ultra-sharp pinnacles sculpted by natural convective dissolution, Proc. Natl. Acad. Sci. USA **117**, 23339 (2020).

[20] D. Lohse and X. Zhang, Physicochemical hydrodynamics of droplets out of equilibrium, Nat. Rev. Phys. **2**, 426 (2020).

[21] N. S. Dhaidan and J. Khodadadi, Melting and convection of phase change materials in different shape containers: A review, Renewable Sustainable Energy Rev. **43**, 449 (2015).

[22] B. Rabbanipour Esfahani, S. C. Hirata, S. Berti, and E. Calzavarini, Basal melting driven by turbulent thermal convection, Phys. Rev. Fluids **3**, 053501 (2018).

[23] B. Favier, J. Purseed, and L. Duchemin, Rayleigh–Bénard convection with a melting boundary, J. Fluid Mech. **858**, 437 (2019).

[24] Z. Wang, L. Jiang, Y. Du, C. Sun, and E. Calzavarini, Ice front shaping by upward convective current, Phys. Rev. Fluids **6**, L091501 (2021).

[25] G. Ahlers, S. Grossmann, and D. Lohse, Heat transfer and large scale dynamics in turbulent Rayleigh-Bénard convection, Rev. Mod. Phys. **81**, 503 (2009).

[26] D. Lohse and K. Xia, Small-Scale Properties of Turbulent Rayleigh-Bénard Convection, Annu. Rev. Fluid Mech. **42**, 335 (2010).

[27] F. Chillà and J. Schumacher, New perspectives in turbulent Rayleigh-Bénard convection, Eur. Phys. J. E **35**, 58 (2012).

[28] O. Shishkina, Rayleigh-Bénard convection: The container shape matters, Phys. Rev. Fluids **6**, 090502 (2021).

[29] S. H. Davis, U. Müller, and C. Dietsche, Pattern selection in single-component systems coupling Bénard convection and solidification, J. Fluid Mech. **144**, 133 (1984).

[30] C. Dietsche and U. Müller, Influence of Bénard convection on solid–liquid interfaces, J. Fluid Mech. **161**, 249 (1985).

[31] Z. Wang, E. Calzavarini, C. Sun, and F. Toschi, How the growth of ice depends on the fluid dynamics underneath, Proc. Natl. Acad. Sci. USA **118**, 10 (2021).

[32] O. Shishkina, Momentum and heat transport scalings in laminar vertical convection, Phys. Rev. E **93**, 051102(R) (2016).

[33] Q. Wang, H.-R. Liu, R. Verzicco, O. Shishkina, and D. Lohse, Regime transitions in thermally driven high-Rayleigh number vertical convection, J. Fluid Mech. **917**, A6 (2021).

[34] B. Gebhart and J. C. Mollendorf, Buoyancy-induced flows in water under conditions in which density extrema may arise, J. Fluid Mech. **89**, 673 (1978).

[35] V. P. Carey, B. Gebhart, and J. C. Mollendorf, Buoyancy force reversals in vertical natural convection flows in cold water, J. Fluid Mech. **97**, 279 (1980).

[36] V. P. Carey and B. Gebhart, Visualization of the flow adjacent to a vertical ice surface melting in cold pure water, J. Fluid Mech. **107**, 37 (1981).

[37] Z. Wang, E. Calzavarini, and C. Sun, Equilibrium states of the ice-water front in a differentially heated rectangular cell, Europhys. Lett. **135**, 54001 (2021).

[38] B. Gebhart and J. C. Mollendorf, A new density relation for pure and saline water, Deep Sea Res. **24**, 831 (1977).

[39] Q. Wang, Q. Zhou, Z. Wan, and D. Sun, Penetrative turbulent Rayleigh-Bénard convection in two and three dimensions, J. Fluid Mech. **870**, 718 (2019).

[40] Q. Wang, P. Reiter, D. Lohse, and O. Shishkina, Universal properties of penetrative turbulent Rayleigh-Bénard convection, Phys. Rev. Fluids **6**, 063502 (2021).

[41] W. J. Boettinger, J. A. Warren, C. Beckermann, and A. Karma, Phase-field simulation of solidification, Annu. Rev. Mater. Res. **32**, 163 (2002).

[42] S. L. Wang, R. F. Sekerka, A. A. Wheeler, B. T. Murray, S. R. Coriell, R. J. Braun, and G. B. McFadden, Thermodynamically-consistent phase-field models for solidification, Physica D **69**, 189 (1993).

[43] E. D. Skyllingstad and C. A. Paulson, A numerical study of melt ponds, J. Geophys. Res. **112**, C08015 (2007).

[44] P. Taylor and D. Feltham, A model of melt pond evolution on sea ice, J. Geophys. Res. **109**, C12007 (2004).

[45] A. FitzMaurice, C. Cenedese, and F. Straneo, A laboratory study of iceberg side melting in vertically sheared flows, J. Phys. Oceanogr. **48**, 1367 (2018).

[46] See Supplemental Material at http://link.aps.org/supplemental/10.1103/PhysRevFluids.7.083503 for movies showing of ice melting under different heating temperatures.

[47] L. Zwirner, A. Tilgner, and O. Shishkina, Elliptical Instability and Multiple-Roll Flow Modes of the Large-Scale Circulation in Confined Turbulent Rayleigh-Bénard Convection, Phys. Rev. Lett. **125**, 054502 (2020).

[48] G. Veronis, Penetrative Convection, Astrophys. J. **137**, 641 (1963).

[49] D. R. Hewitt, J. A. Neufeld, and J. R. Lister, Convective shutdown in a porous medium at high Rayleigh number, J. Fluid Mech. **719**, 551 (2013).

[50] S. Manabe and R. J. Stouffer, Simulation of abrupt climate change induced by freshwater input to the North Atlantic Ocean, Nature (London) **378**, 165 (1995).

[51] M. Ghil and V. Lucarini, The physics of climate variability and climate change, Rev. Mod. Phys. **92**, 035002 (2020).